J Mater Sci (2017) 52:858–868

Silicon particle pinhole defects in aluminium–silicon alloys

Martin Guillermo Mueller[1,*], M. Fornabaio[1], and A. Mortensen[1]

[1] Laboratory of Mechanical Metallurgy, Institute of Materials, École Polytechnique Fédérale de Lausanne (EPFL), Station 12, 1015 Lausanne, Switzerland

Received: 16 June 2016
Accepted: 6 September 2016
Published online: 19 September 2016

ABSTRACT

It was recently shown that silicon particles in heat-treated Al–Si casting alloys can contain flaws such as surface pinholes and grooves, which cause varying degrees of reduction in the in situ particle fracture strength and hence influence the mechanical properties of this class of alloys. In this work, we show that the formation of one class of such strength-limiting flaws in solidified and coarsened Si particles, namely surface pinholes, is caused by alloy impurities such as Fe and Ti in both binary eutectic Al–Si alloys and also in casting alloy A356. This is evidenced by using Focused Ion Beam serial sectioning tomography coupled with Energy-Dispersive X-Ray Spectroscopy, and confirmed by the observation that a high-purity Al–Si alloy presents a significantly lower proportion of pinholes along the surface of the silicon phase than does an alloy of commercial purity. A similar correlation between alloy purity and the formation of another, more severe strength-limiting particle defect, namely grooved interfaces, was on the other hand not found.

Introduction

Silicon particles play a key role in the solidification, microstructural development and fracture processes of Al–Si-based alloys [1–9]. When these alloys are mechanically strained, it is typically observed that silicon particles within the α-aluminium matrix start fracturing gradually, essentially as soon as the alloy starts to deform plastically. As the number of fractured particles increases, nucleated microcracks start to grow, and then link by tearing the aluminium matrix that connects fractured silicon particles. This lowers the rate of work hardening of the alloy, in turn hastening the onset of the tensile instability; also, the coalescence of such microcracks produces macrocracks that can drive final fracture of the material. Since most aluminium casting alloys contain significant proportions of silicon, it is important to understand what determines the strength of silicon particles contained in these alloys, and to identify pathways to strengthen those particles.

Traditional approaches used to measure the strength of silicon particles in aluminium are almost exclusively indirect. In one approach, the average stress in the particles as a function of macroscopic alloy strain is calculated through micromechanical

Address correspondence to E-mail: martin.mueller@epfl.ch

DOI 10.1007/s10853-016-0381-y

models and related to the measured proportion of fractured particles [1, 10, 11]. In another approach, X-ray or neutron diffraction techniques are used to measure the local average stress state of silicon particles within an alloy that is subjected in situ to a tensile test [12, 13]. These approaches have provided insight on microstructure–property relationships of several of these alloys; however, they do not identify underlying reasons why the silicon particles are as weak—or strong—as they are found to be. The reason is that those techniques assess average properties of a large number of silicon particles, which are furthermore only characterised using average microstructural parameters such as the size and aspect ratio of the particle population.

In recent work, the strength of individual silicon particles was measured directly using a novel microscopic 3-point bending technique [14]. This approach treats individual particles as separate samples of material, each with their own microstructure and strength-limiting flaws. The probed particles, which were extracted from a coarsened eutectic Al–Si alloy by deep-etching, could be classified into two groups: (i) those in which the surface subjected to tensile stress contained no pre-identified defects, and (ii) those that had a distinct microstructural defect visible along the tested surface (see Fig. 5 of Ref. [14]). Results show that silicon particles from the first group have very high local strength values, commensurate with strength values found in specimens of the same size produced from electronic grade silicon [15], *i.e.* on the order of 9 GPa and thus approaching the theoretical strength of silicon. Particles from the second group were, on the other hand, found to be much weaker [14]. The implication is that silicon particles within Al–Si casting alloys can be very strong, but many of them feature defects along their surface that strongly reduce the particle strength, notably because they act as stress concentrators.

Examples of silicon particles in binary Al–12.6 %Si and A356 alloys in either the as-cast or heat-treated conditions are shown in Fig. 1. The presence of defects on the particles such as surface holes or "pinholes" of various sizes (indicated with white arrows), surface step- or groove-like interfaces, burrs and necks is evident along the particle surfaces, in both alloy conditions. Fig. 2 shows fractured silicon

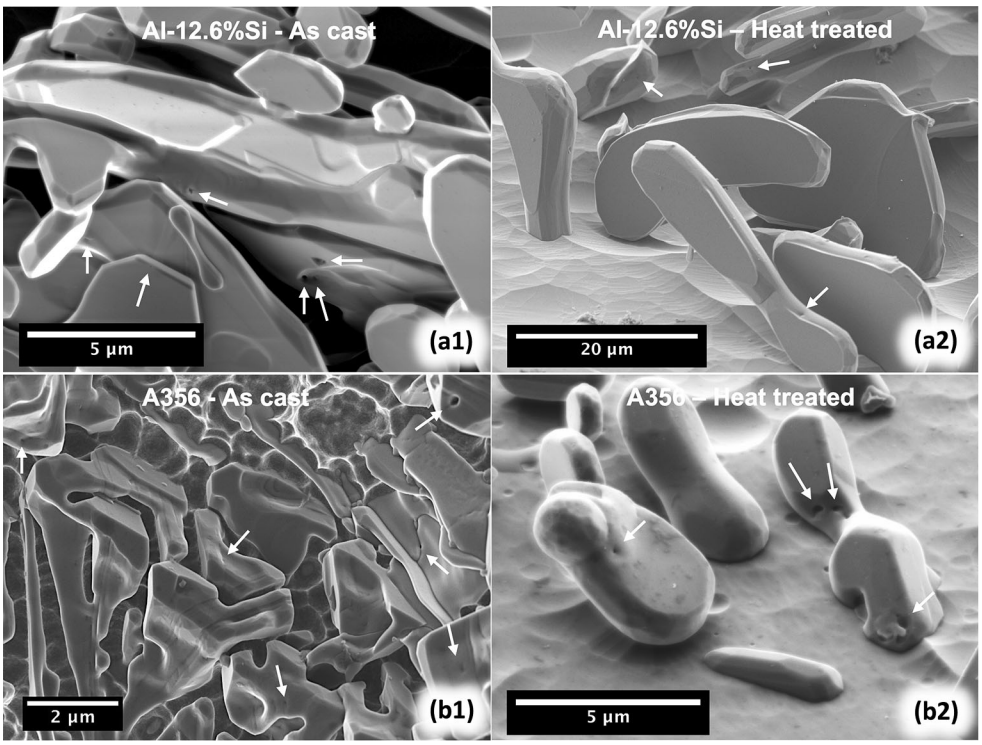

Figure 1 SEM images of silicon particles from a Al-12.6 %Si alloy (**a**1–**a**2) and from alloy A356 (**b**1–**b**2) exposed by selectively dissolving the aluminium matrix of the alloys in either the as-cast or heat-treated conditions. Several defects on the particles are observable (see main text); among them pinholes are indicated with *white arrows*.

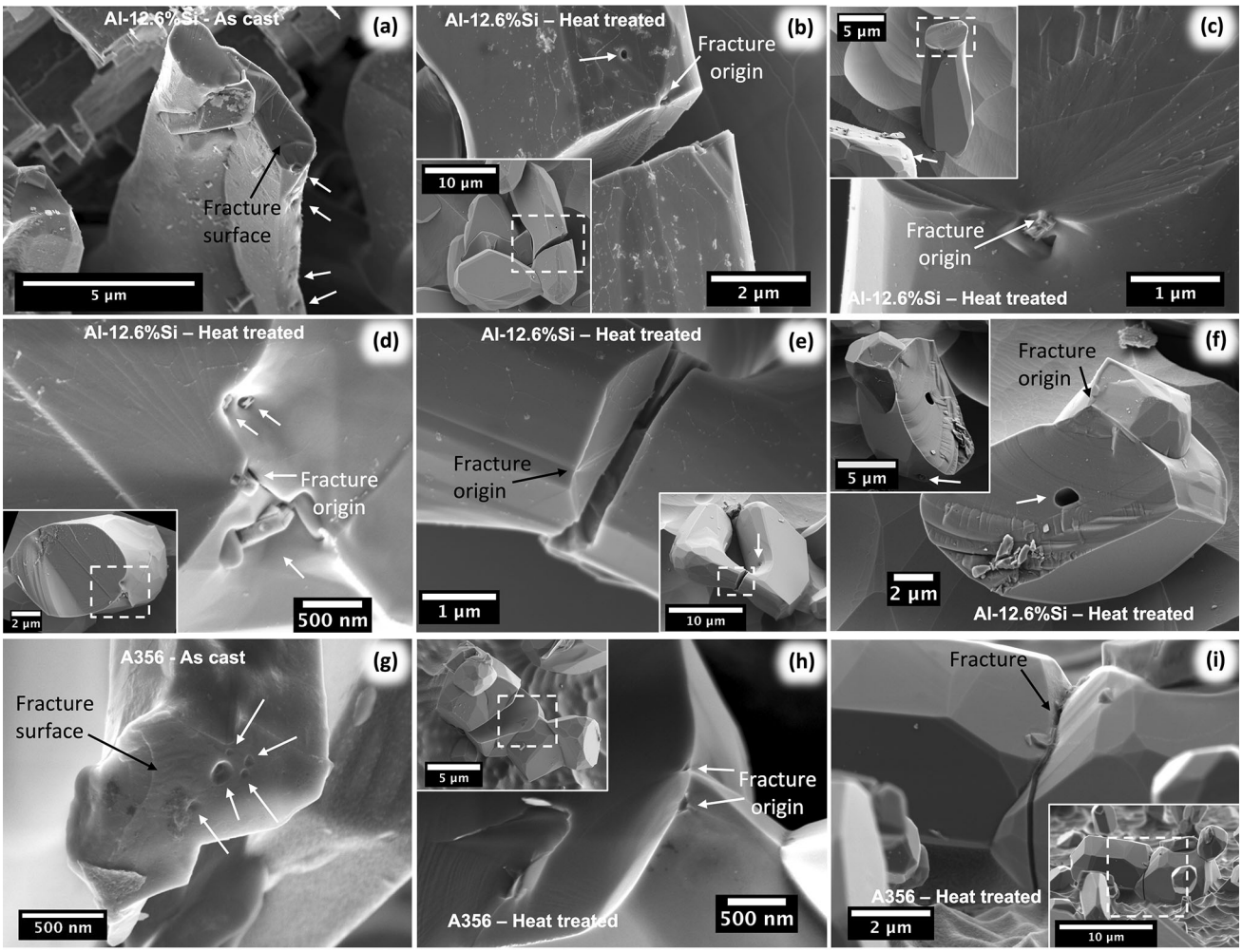

Figure 2 Fractured silicon particles from Al-12.6 %Si and alloy A356, in the as-cast and heat-treated conditions. The alloy samples were deformed in tension, followed by aluminium selective etching to expose the silicon particles for subsequent examination in the SEM. Surface pinholes (or similar surface defects) and internal cavities along fracture surfaces are indicated with *white arrows*. In the *insets*, a lower magnification image of the fractured particle is shown. In most particles, the fracture origin can be identified and is found to be a stress-concentrating defect on the silicon particles: pinholes in **a**, **b**, **c**, **d** and **h**, a shallow-groove linked to a twin boundary in **e** and deep grooved interfaces in **f** and **i**.

particles from macroscopic specimens of each alloy, in either condition, which were deformed in tension before selectively deep-etching the aluminium phase for Scanning Electron Microscopic (SEM) examination of the particles. Surface pinholes and internal "cavities" (the latter seen along the fracture surfaces in Fig. 2f, g) are here too indicated with white arrows. In most of these particles, the fracture origin can be identified by examining the beach-marks and/or by following the river pattern on the particle fracture surface: these point to a stress-concentrating defect along the particle surface. Pinholes (or similar defects) were the fracture origin of particles in Fig. 2b–d, h and, arguably, Fig. 2a. The particle in Fig. 2e fractured at a location situated along a neck (see low-magnification image in the inset); here, the precise fracture origin is a shallow surface groove, which is likely related to a twin plane. The particles in Fig. 2f and 2i broke at interfaces, the latter a deeply grooved one. All those flaws are important factors affecting the strength of the silicon particles within the alloy, and hence govern in turn the strength or toughness of the Al–Si-based alloy.

SEM examination of defects on silicon particles such as those in Ref. [14] and in Figs. 1 and 2 was made possible after subjecting each alloy to a deep-etching procedure, so as to selectively dissolve the primary aluminium phase over a depth of a few

micrometres and expose silicon particles that were present within the microstructure. Even though the etching procedures, described in the next section, are generally known to be harmless to silicon (other than producing some nanometer-thick surface oxidation, see the discussion in Sect. 4.3 of Ref. [14]), it is not granted that the surface defects observed on silicon particles after etching were not modified by the etching procedure, particularly if they were the seat of (removed) variations in the composition of the particle or if the defects neighboured second phases that were also dissolved. In the extreme, pinholes might even be suspected to be the result of a pitting corrosion mechanism during the deep-etching procedure, rather than being intrinsic particle defects.

To alleviate the limitations and concerns linked to the use of an etching procedure, in this work we investigate the (strength-limiting) Si particle defects identified earlier using Focused Ion Beam (FIB)-tomographic examination of the microstructures within polished samples of two Al–Si alloys. Results reveal the presence of small intermetallic particles at the root of surface pinholes and in internal "cavities" within the silicon particles. Other defects, namely grooves and burrs, are on the other hand not linked to such impurities. To corroborate that surface pinholes are the result of the presence of impurities, an Al–Si alloy of very high purity was also produced and compared to a lower purity alloy using a statistical survey of defects found along exposed Si particles.

Materials and methods

Two alloys, namely a binary eutectic Al–12.6 %Si alloy—also referred to as a *standard-purity* eutectic alloy—and a A356 alloy, were used to examine the silicon particles within their microstructure using FIB-tomography coupled with Energy-Dispersive X-ray Spectroscopy (EDXS) analysis. The chemical composition of these two alloys is given in Table 1. For Al-12.6 %Si, the as-cast condition refers to the state in which it was delivered by the producer, Alusuisse Technology & Management AG (Neuhausen am Rheinfall, Switzerland), within cast ingots roughly 40 cm × 9 cm × 2 cm in size. The heat-treated condition refers for this alloy to exposure for 7 days to 550 °C, a heat-treatment that was conducted with a goal to coarsen the silicon particles.

Table 1 Chemical composition in wt% of the alloys used in this work for FIB-tomography and EDX examination

Alloy	Si	Mg	Cu	Fe	Mn	Cr	Ni	Ti	Zn	Other (total)	Al
Al-12.6 %Si	12.6 ± 0.4	<0.003	<0.003	0.033 ± 0.002	<0.003	<0.003	<0.003	<0.003	<0.003		Bal
A356	6.5–7.5	0.25–0.45	0.2 max	0.2 max	0.1 max	0.05 max	0.05 max	0.2 max	0.1 max	0.15 max	Bal

Table 2 Chemical composition in ppm of the 5N6 aluminium used, together with high-purity silicon, to produce the high-purity Al-12.6 %Si alloy

Li	<0.002	Ti	0.14	Fe	0.26	As	<0.009	Sb	<0.009	Ca	<0.2
B	0.019	V	0.056	Ni	<0.004	Zr	0.018	La	0.0056	Si	1.4
Mg	0.92	Cr	0.11	Cu	0.24	Ag	<0.01	Ce	0.041	Al	Bal
P	0.056	Mn	0.087	Zn	<0.01	Sn	<0.02	Na	<0.1		

The A356 alloy (from Alu Metall Guss AG, Gontenschwil, Switzerland) was cast by ourselves into a copper permanent mould producing a rod 15 cm high and 2 cm in diameter. Its heat-treatment was conducted at 540 °C during 6 h, followed by air cooling.

The FIB-tomographic examination was carried out along the surface of polished samples of the two alloys described above, in either the as-cast or heat-treated conditions. Progressive cross sections of silicon particles and their surrounding aluminium matrix were produced by ion-milling using 30 kV Ga^+ ions and imaged using a secondary electron in-lens detector (which gives contrast based particularly on the electronic properties of the elements in a given phase). The apparatus used was a Zeiss™ NVision™ 40 (Oberkochen, Germany) SEM/FIB dual-beam system. Local chemical analyses were conducted using qualitative EDXS at an electron acceleration voltage of 10 kV to identify the chemical elements of the observed phases (80 mm^2 X-Max™ silicon drift detector from Oxford Instruments, Tubney Wood, Abingdon, Oxfordshire, UK). No automated FIB milling methods were used in this work; instead, the SEM/FIB operator controlled the progressive sectioning. In this way, the thickness of each successive section could be adjusted (between about 100 nm up to about 700 nm) according to the observed presence or absence of interesting features within the particle under investigation. When a defect was spotted, its nature (i.e. whether it was a surface pinhole or a surface grooved interface for example) could be deduced by the analysis of successive cross sections.

Moreover, a control experiment was performed with a goal to compare the occurrence frequency of pinholes on the silicon particles of the standard-purity eutectic alloy with that of this type of defects on the particles of a *high-purity* eutectic alloy (as shown in the next sections, the main finding of this work is that impurities cause pinholes on silicon particles). This high-purity eutectic alloy was produced in an induction furnace under an argon atmosphere using a carbon crucible and a steel mould 15 cm tall of 2 × 2 cm square cross section. The mould was open at the bottom, where a large copper piece was attached for enhanced heat extraction by direct contact with the solidifying alloy. The crucible and the mould were beforehand coated with boron nitride. The raw materials were 5N6 aluminium (from Alcoa, Pittsburgh PR, USA) (see its chemical analysis in Table 2) mixed with 12.6 wt% of polycrystalline silicon flakes of purity 5 N or higher (from Wacker Chemie AG, Munich, Germany). The temperature, measured on the crucible, was cycled 4 times between 650 °C and 900 °C to enhance dissolution of the silicon flakes and to homogenise the melt before casting at 800 °C. The alloy was subsequently heat-treated in the same way as the standard-purity Al-12.6 %Si alloy (i.e. 7 days at 550 °C).

The control experiment consisted in individually examining, using the SEM, 225 silicon particles extracted from each of the standard-purity or the high-purity eutectic alloys in the heat-treated condition, and then counting how many of them featured pinhole defects on their visible surfaces. Results from the same measurement conducted with the standard-purity alloy have already been reported in Ref. [14].

The procedure used to extract particles from the alloys and to place them along a flat surface is described in detail in Ref. [14]. In summary, it is based on chemical etching (using a solution prepared with H_3PO_4 85 %, CH_3COOH 100 % and HNO_3 70 % mixed in volume ratio 83:5.5:5.5) or electro-chemical etching (using HNO_3 6.5 % or NaCl in water as electrolyte) to selectively dissolve the aluminium matrix, then filtering the solution containing extracted particles by passing it through a filter paper to recover the particles, washing them with deionised water and ethanol and finally spreading them on a flat substrate that could be brought to the SEM after drying.

Results

FIB-tomography

In the heat-treated standard-purity Al-12.6 %Si alloy, a total of 14 silicon particles embedded within the

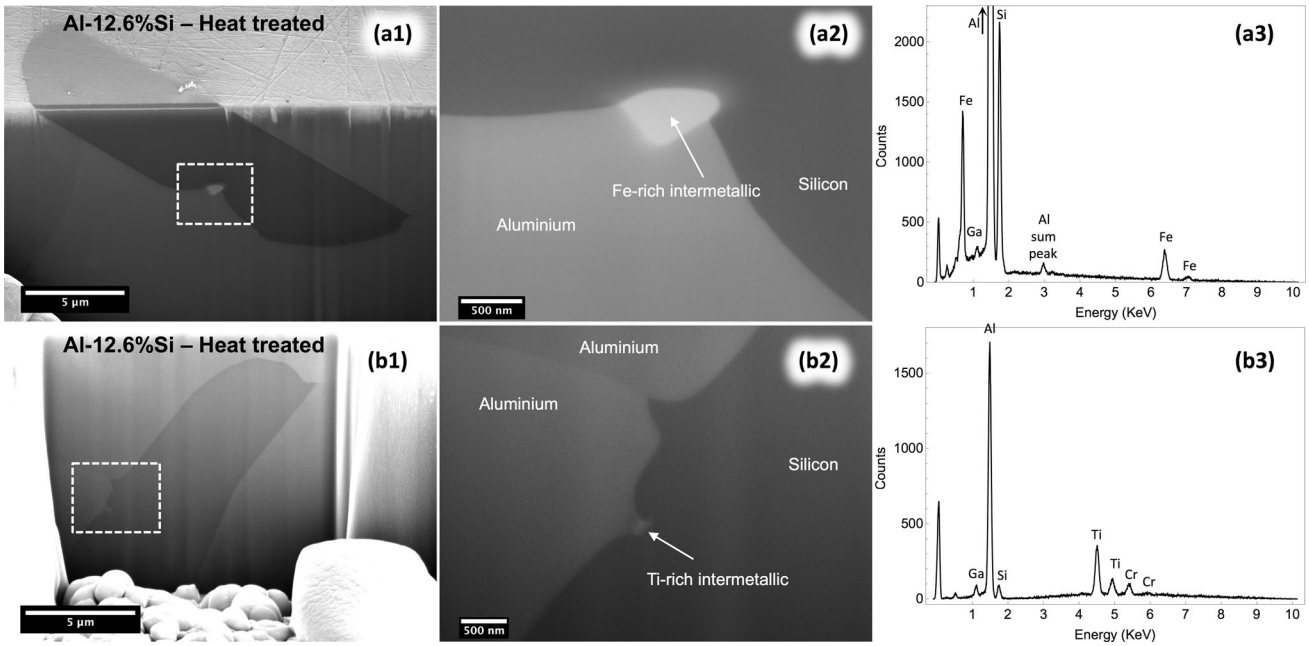

Figure 3 SEM images obtained from cross sections of silicon particles embedded within the primary aluminium phase, produced by FIB milling. The alloy is Al-12.6 %Si. Images **a**2 and **b**2 are close-ups of the area indicated in **a**1 and **b**1, respectively, which correspond to pinholes on the surface of the silicon particles. EDX spectra **a**3 and **b**3 correspond to the intermetallic particles indicated with *an arrow* on images **a**2 and **b**2, respectively. In images **b**1 and **b**2, a *burr-like ridge* on the silicon surface can also be observed.

aluminium matrix were partially or fully sectioned using FIB-tomography. In 6 of those 14 silicon particles, a Fe-rich intermetallic particle containing also Al and Si and having submicronic dimensions was found at the bottom of what could be identified as a metal-filled surface hole (or "pinhole"); Fig. 3a gives an example. Also, in this alloy no such Fe-rich particle was found to be fully encapsulated by a silicon particle, and only one was found to be surrounded by aluminium (*i.e.* not to be in contact with Si).

In the same sample, ten other small intermetallic particles containing Al, Ti and Cr were also found; two of these were located at the root of surface pinholes on silicon particles (one is shown in Fig. 3b). Of the remaining eight intermetallic particles, seven were located inside silicon particles, while one was embedded within the aluminium-rich phase. These particles were even smaller than the Fe-rich intermetallic particles mentioned above: their size was on the order of 100 nm. Given their small size, it is likely that many other particles of this kind were missed due to the relative thick sectioning that was used. On their EDXS spectra, a small peak corresponding to Si was also present; however, it is not possible to tell whether that Si signal originated from the small intermetallic particle, from the silicon particle around it or whether it is simply an artefact (*e.g.* an internal fluorescence peak).

Intermetallic particles similarly located within surface pinholes or fully embedded inside silicon particles were also found in the heat-treated A356 alloy. Several Fe-rich particles of size on the order of 100 nm were found to be fully embedded within different silicon particles; one example is shown in Fig. 4a1 and the corresponding EDXS spectrum of the Fe-rich particle is given in Fig. 4a2. The cavities on the fracture surface of a silicon particle of this alloy shown in Fig. 2g are possibly linked to such nanoscopic Fe-rich internal precipitates, which disappeared together with the aluminium matrix during the etching procedure. Moreover, Fig. 4b1 shows a Ti-rich intermetallic particle within a surface hole on a silicon particle. In Fig. 4b2, the EDXS spectrum of the intermetallic particle shows the presence of Ti, V and arguably some Ni. Measured Al, Si and Mg peaks could come from the intermetallic particle, but potentially also from the phases around it (the silicon particle and the aluminium matrix). We note in passing that a particle smaller than 100 nm with its EDXS spectrum showing the presence of P, Al, Si and

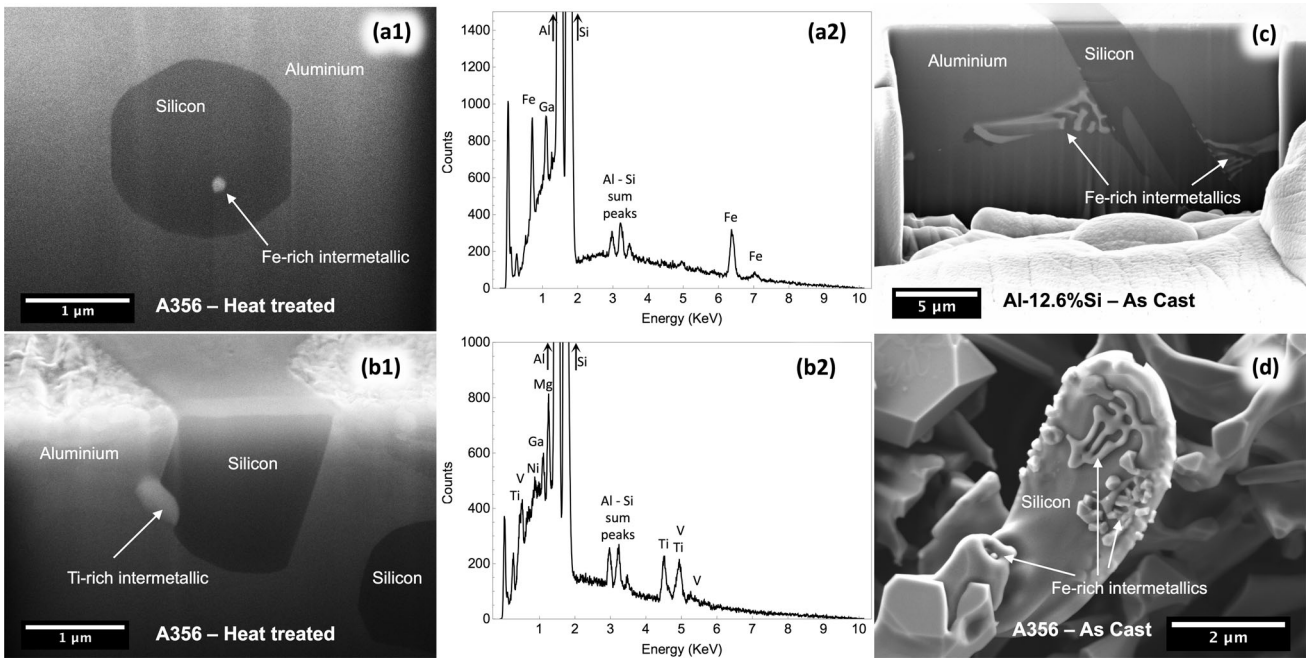

Figure 4 **a–c** SEM images of silicon particles within the aluminium–silicon alloys obtained from cross sections produced by FIB milling. **a**1 and **b**1 show an intermetallic particle inside silicon and in a surface feature, respectively, in a A356 heat-treated alloy. **a**2 and **b**2 are the EDX spectra corresponding the intermetallic particles indicated with *an arrow* in **a**1 and **b**1, respectively. **c** Cross section of a silicon particle within aluminium showing the presence of irregular (eutectic) Fe-rich intermetallic phase in the as-cast Al-12.6 %Si alloy. **d** SEM image of a silicon particle extracted by deep-etching from the as-cast A356 alloy showing irregular (eutectic) Fe-rich intermetallic phase on its surface and in a shallow pinhole defect.

Mg was found within a silicon particle (data not shown); this could be a particle onto which silicon nucleated heterogeneously [16–18].

FIB-tomographic examinations were also done on the standard-purity Al-12.6 %Si alloy in the as-cast condition. There again, Fe-rich intermetallics were found to be connected to silicon particles; however, in this condition their shape was very irregular, see Fig. 4c. Similarly, Fig. 4d shows a silicon particle of the as-cast A356 alloy featuring irregular Fe-rich intermetallic particles, both along its surface and within a surface hole.

Such irregular intermetallic particle shapes were not observed in the heat-treated alloys, indicating that the intermetallic phases also undergo strong morphological changes upon heat-treatment (as do silicon particles). We note in passing that Fe- or Ti-rich intermetallics were not easy to find on silicon particles after deep-etching, suggesting that the intermetallics are mostly removed together with the aluminium matrix in the etching process. In other words, structures such as that in Fig. 4d were a rather rare occurrence after deep-etching; instead, silicon surface pinholes are generally found to be empty when an etching procedure is used to extract and examine the silicon phase.

Apart from surface pinholes and internal defects, we identified and examined eight groove- or step-like defects and four ridge-like features (or "burrs") on the Al–Si interface of different embedded silicon particles of both alloys after heat-treatment. An example of a groove-/step-like interface is shown in Fig. 5, where the white arrows indicate the defect along successive sections. Two examples of burrs can be observed in the cross section shown in Fig. 3b1, one of which is magnified in Fig. 3b2. Along such embedded surface grooves, steps or ridges, nothing but aluminium and silicon were detected.

Control experiment

A statistical comparison between the occurrence frequency of pinholes between high-purity and standard-purity eutectic binary Al–Si alloys was also conducted as a control experiment. Particles extracted by deep-etching from either alloy and spread on a flat substrate were examined one by one with the SEM to check whether they had any pinhole on their

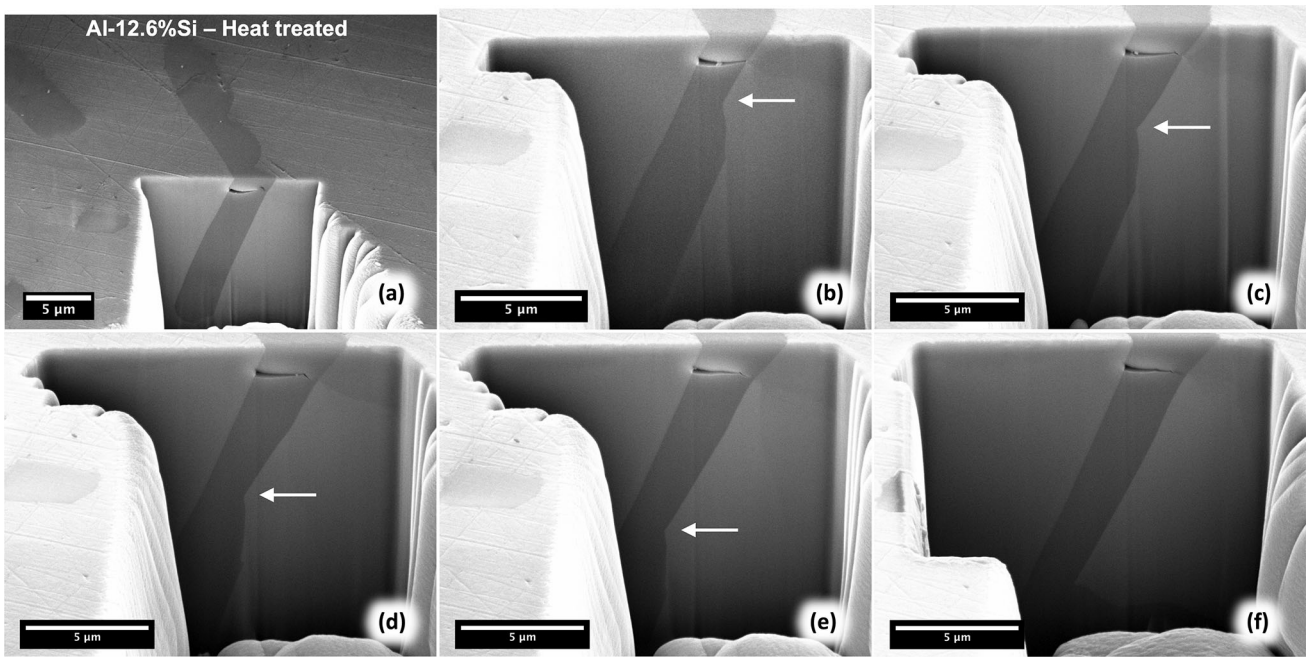

Figure 5 **a**–**f** Successive cross sections produced by FIB milling of a silicon particle within aluminium, imaged using SEM. The *white arrows* indicate a groove-/step-like interface; here, no intermetallic particle became apparent.

SEM-accessible surfaces. It was found that 32 % of the particles from the standard-purity alloy feature at least one surface pinhole [14], while only 6 % of the particles from the high-purity alloy do. Note that these numbers underestimate the actual proportion of particles featuring pinholes because particle facets in contact with the flat substrate were not accessible for SEM examination and it was therefore impossible to know whether pinholes were present on those facets or not. Such bias, nevertheless, is similar for both alloys and thus the observed difference between them is conclusive.

Discussion

The FIB-tomography investigation shows conclusively that, at the root of surface pinholes and inside internal defects of silicon particles, there are Fe-rich or Ti-rich intermetallics. Moreover, the control experiment shows that far fewer pinholes exist along the surface of silicon particles within a high-purity alloy compared to a standard-purity alloy, which further demonstrates the link between the occurrence of those flaws and the presence of Fe- or Ti-containing intermetallic second phases. Fe and Ti impurities are therefore linked with the formation of this particular strength-reducing Si particle defect. Whether this is one of the main mechanisms by which those impurities reduce the mechanical properties of aluminium casting alloys could, on the other hand, not be determined here, for two reasons: (i) these impurities exert other influences on the alloy microstructure (e.g. they also appear as large brittle intermetallic particles and can affect the Si particle size and distribution), and (ii) there are other, more strongly strength-limiting, defects in Si particles that do not seem to be triggered by the presence of Fe, Ti or other impurities. Grooves, which are shown here not to be correlated with the presence of intermetallic precipitates, are one important example.

In Al–Si alloys, Fe-rich intermetallics are virtually always present to some degree: Fe, which has very limited solid solubility [19, 20] in aluminium alloys, is one of the main alloy impurities (it is sometimes also used as a deliberate alloying element in hypereutectic Al–Si alloys [24]). The most common and important known Fe-intermetallic is the β-Al_5FeSi phase. This normally forms large and elongated platelets [21], which are at times connected, at times not, to silicon particles [22] and are known to severely reduce the alloy ductility [23]. Another common Fe-containing phase is the α-Al_8Fe_2Si intermetallic, which has a Chinese-script morphology [19]. Also small Fe-rich particles (closer to those observed in the present work) have been observed before using Electron Back-Scatter Diffraction in Al–Si alloys [25, 26]. In

fact, there are many other intermetallic phases that can form in the Al–Si–Fe system [19, 27, 28] and their number increases significantly when other alloying elements such as Cu, Mg, Mn, Ti or Ni are present [28, 29]. We have not sought here to identify the exact crystallographic nature of the various small intermetallic particles that were found within silicon particle pinholes, in part because there is uncertainty on their composition with the method used here: quantitative EDXS results can be affected by the surrounding phases, given the small size of the intermetallic particles compared to the interaction volume of 10 kV electrons.

Ti, Cr and V are impurities normally found in aluminium alloys, though in lesser proportion than Fe. In particular, Ti is widely used for grain refinement, notably through added Al–Ti–B grain-refining master alloys [30]. Even though the exact mechanisms of grain refinement in aluminium wrought and casting alloys are not yet fully understood, it is known that operative phases are $TiAl_3$ and TiB_2 [31, 32] (the EDXS analysis in this work unfortunately cannot detect B). A number of intermetallic phases containing different combinations of Ti, Cr, Zr, V, Al, Si, Mg and Cu have also been identified in a recent study on an Al–Si casting alloy [33]; this is in line with our findings of Ti–Cr and Ti–V together with Al forming intermetallic phases in the present alloy.

It is interesting that small particles such as those Fe- or Ti-containing intermetallics are able to pin the Al–Si interface so strongly as to form circular holes that are, at times, many particle diameters deep, see Figs. 1, 2 and 3. Likely, this betrays values of the interfacial energy between those intermetallics and silicon that exceed the interfacial energy between those intermetallics and aluminium (2D "contact angles" of Si on the intermetallic, Figs. 3 and 4, suggest this; note, however, that one must be careful with the transposition to 3D of values measured along individual 2D sections). Another cause for the formation of relatively deep pinholes might be the likely anisotropic distribution of the solid Al–Si interfacial energy with interface orientation. This will in turn create torque terms, which could prevent Al–Si interfaces from meeting to engulf intermetallic nanoparticles within the much larger coarsening Si particles.

Another feature that can be noted, particularly on the edges of coarsened silicon particles, is ridges resembling burrs, Fig. 1a2. Their presence is easily explained as a result of local capillary equilibration along the triple line formed where an aluminium grain boundary meets the Al–Si interface; see Fig. 3b1–b2. With Al–Si interfacial energies on the order of 0.26–0.40 J/m^2 (from the values for Si with liquid aluminium at the eutectic temperature [34–36]) and aluminium grain boundary energies roughly between 0.2 and 0.6 J/m^2 [37, 38], given the long hold times and high temperatures of heat-treatment, the formation of broad ridges characteristic of equilibration with a finite dihedral angle in the middle of the range between 0 and 180° makes sense. Along the linear burr-like ridges no intermetallic particles were observed; this was also the case for the grooves and the steps. While it remains a possibility that impurities smaller than can be caught at the resolution of the present technique (i.e. in the order of a couple of tens of nanometers) might actually exist there, there is a clear difference between what was found along these kinds of defects, and what was found at the bottom of surface pinholes, where intermetallic particles were readily visible and could be identified as the cause underlying formation of that particular class of strength-limiting silicon particle defect.

Conclusions

In conclusion, we complement here a previous contribution [14] in which we measured the strength of individual silicon particles from an Al–Si alloy and showed that there are identifiable, specific defects that weaken Si particles in aluminium casting alloys. We demonstrate here, using FIB-tomography and EDXS examination of Al-12.6 %Si and A356 alloys, the following:

(i) Burr-like defects exist on the edges of some coarsened silicon particles. These are a consequence of capillary force equilibration where aluminium grain boundaries meet the particles (and are not associated with the presence of other second phases).
(ii) Groove- and step-like defects on silicon particles are also not linked to impurity-containing intermetallic particles, so their existence might instead be related to mechanisms of Si particle growth or coarsening.
(iii) Pinholes found along the surface of etched silicon particles are not voids but contain, at their root, submicronic Fe-rich or Ti-rich

intermetallic particles, and are otherwise filled before etching with the aluminium-rich primary phase.

The well-known deleterious influence of impurities in aluminium casting alloys is thus twofold: not only are impurity-containing intermetallics weak second phases that promote the early onset of internal damage, but they also form stress-concentrating "pinhole" defects that contribute, together with other silicon particle defects found here not to be connected to those impurities, to decrease the silicon particle fracture strength to values below the ideal strength of Si.

Acknowledgements

This research was funded by the European Research Council under the European Union's Seventh Framework Programme (FP/2007-2013)/ERC Advanced Grant Agreement No. 291085. Scanning electron microscopy, focused ion beam milling and energy-dispersive X-ray spectroscopy were performed at the Interdisciplinary Centre of Electron Microscopy at the Ecole Polytechnique Fédérale de Lausanne (CIME-EPFL). The authors would like to thank Dr. Marco Cantoni of the CIME-EPFL for helpful discussions on the EDXS results.

Compliance with ethical standards

Conflicts of interest The authors declare that they have no conflict of interest.

References

[1] Caceres CH, Griffiths JR (1996) Damage by the cracking of silicon particles in an Al-7Si-0.4 Mg casting alloy. Acta Mater 44:25–33. doi:10.1016/1359-6454(95)00172-8

[2] Lebyodkin M, Deschamps A, Bréchet Y (1997) Influence of second-phase morphology and topology on mechanical and fracture properties of Al–Si alloys. Mater Sci Eng A 234–236:481–484. doi:10.1016/S0921-5093(97)00314-6

[3] Doglione R, Douziech JL, Berdin C, François D (2002) Tensile damage stages in cast A356-T6 aluminium alloy. Mater Sci Technol 18:554–562. doi:10.1179/026708302225001660

[4] Cerri E (2004) Damage and plastic flow in a Al–Si–Cu thixocast alloy. J Mater Sci 39:3115–3119. doi:10.1023/B:JMSC.0000025840.44871.ff

[5] Zhu M, Jian Z, Yao L et al (2010) Effect of mischmetal modification treatment on the microstructure, tensile properties, and fracture behavior of Al-7.0 %Si-0.3 %Mg foundry aluminum alloys. J Mater Sci 46:2685–2694. doi:10.1007/s10853-010-5135-7

[6] Ammar HR, Samuel AM, Samuel FH, Al-Ahmari AMA (2011) Aging behavior of 359-type Al–9 %Si–0.5 %Mg casting alloys. J Mater Sci 47:1331–1338. doi:10.1007/s10853-011-5906-9

[7] Requena G, Garcés G, Asghar Z et al (2011) The effect of the connectivity of rigid phases on strength of Al–Si Alloys. Adv Eng Mater 13:674–684. doi:10.1002/adem.201000292

[8] Doglione R (2012) In situ investigations on the ductility of an Al–Si–Mg casting alloy. JOM 64:51–57. doi:10.1007/s11837-011-0231-y

[9] Joseph S, Tewari A, Kumar S (2012) The fracture characteristics of a near eutectic Al–Si based alloy under compression. Metall Mater Trans A 44:2358–2368. doi:10.1007/s11661-012-1580-z

[10] Wang QG, Caceres CH, Griffiths JR (2003) Damage by eutectic particle cracking in aluminum casting alloys A356/357. Metall Mater Trans A 34:2901–2912. doi:10.1007/s11661-003-0190-1

[11] Kiser MT, Zok FW, Wilkinson DS (1996) Plastic flow and fracture of a particulate metal matrix composite. Acta Mater 44:3465–3476. doi:10.1016/1359-6454(96)00028-6

[12] Coade RW, Griffiths JR, Parker BA, Stevens PJ (1981) Inclusion stresses in a two-phase alloy deformed to a plastic strain of 1 %. Philos Mag A 44:357–372. doi:10.1080/01418618108239538

[13] Finlayson TR, Griffiths JR, Viano D et al (2007) Stresses in the eutectic silicon particles of strontium-modified A356 castings loaded in tension. In: Crepeau PN, Tiryakioglu M, Campbell J (eds) Shape Casting: 2nd International Symposium. TMS (The Minerals, Metals & Materials Society), Warrendale, pp 127–134

[14] Mueller MG, Fornabaio M, Žagar G, Mortensen A (2016) Microscopic strength of silicon particles in an aluminium–

silicon alloy. Acta Mater 105:165–175. doi:10.1016/j.actamat.2015.12.006

[15] Namazu T, Isono Y, Tanaka T (2000) Evaluation of size effect on mechanical properties of single crystal silicon by nanoscale bending test using AFM. J Microelectromechanical Syst 9:450–459. doi:10.1109/84.896765

[16] Ho CR, Cantor B (1995) Heterogeneous nucleation of solidification of Si in Al–Si and Al–Si–P alloys. Acta Metall Mater 43:3231–3246. doi:10.1016/0956-7151(94)00480-6

[17] Nogita K, McDonald SD, Tsujimoto K et al (2004) Aluminium phosphide as a eutectic grain nucleus in hypoeutectic Al–Si alloys. J Electron Microsc (Tokyo) 53:361–369. doi:10.1093/jmicro/dfh048

[18] Liang S-M, Schmid-Fetzer R (2014) Nucleants of Eutectic Silicon in Al–Si Hypoeutectic Alloys: β-(Al, Fe, Si) or AlP Phase. Metall Mater Trans A 45:5308–5312. doi:10.1007/s11661-014-2522-8

[19] Lu L, Dahle AK (2005) Iron-rich intermetallic phases and their role in casting defect formation in hypoeutectic Al–Si alloys. Metall Mater Trans A 36:819–835. doi:10.1007/s11661-005-1012-4

[20] Zhang L, Gao J, Damoah LNW, Robertson DG (2012) Removal of iron from Aluminum: a review. Miner Process Extr Metall Rev 33:99–157. doi:10.1080/08827508.2010.542211

[21] Terzi S, Taylor JA, Cho YH et al (2010) In situ study of nucleation and growth of the irregular α-Al/β-Al5FeSi eutectic by 3-D synchrotron X-ray microtomography. Acta Mater 58:5370–5380. doi:10.1016/j.actamat.2010.06.012

[22] Tang SK, Sritharan T (1998) Morphology of β-AIFeSi intermetallic in AI-7Si alloy castings. Mater Sci Technol 14:738–742. doi:10.1179/mst.1998.14.8.738

[23] Javidani M, Larouche D (2014) Application of cast Al–Si alloys in internal combustion engine components. Int Mater Rev 59:132–158. doi:10.1179/1743280413Y.0000000027

[24] Choi YS, Lee JS, Kim WT, Ra HY (1999) Solidification behavior of Al-Si-Fe alloys and phase transformation of metastable intermetallic compound by heat treatment. J Mater Sci 34:2163–2168. doi:10.1023/A:1004584415196

[25] Shankar S, Riddle YW, Makhlouf MM (2004) Nucleation mechanism of the eutectic phases in aluminum-silicon hypoeutectic alloys. Acta Mater 52:4447–4460. doi:10.1016/j.actamat.2004.05.045

[26] Timpel M, Wanderka N, Murty BS, Banhart J (2010) Three-dimensional visualization of the microstructure development of Sr-modified Al–15Si casting alloy using FIB-EsB tomography. Acta Mater 58:6600–6608. doi:10.1016/j.actamat.2010.08.021

[27] Khalifa W, Samuel FH, Gruzleski JE (2003) Iron intermetallic phases in the Al corner of the Al–Si–Fe system. Metall Mater Trans A 34:807–825. doi:10.1007/s11661-003-0116-y

[28] Li Z, Kuang X, Liao C et al (2015) Phase equilibria of the Al–Fe–Si–Ti quaternary system at 700 °C. J Phase Equilibria Diffus 37:174–185. doi:10.1007/s11669-015-0443-x

[29] Chen C-L, Thomson RC (2010) The combined use of EBSD and EDX analyses for the identification of complex intermetallic phases in multicomponent Al–Si piston alloys. J Alloy Compd 490:293–300. doi:10.1016/j.jallcom.2009.09.181

[30] Mallapur DG, Kori SA, Udupa KR (2010) Influence of Ti, B and Sr on the microstructure and mechanical properties of A356 alloy. J Mater Sci 46:1622–1627. doi:10.1007/s10853-010-4977-3

[31] Kori SA, Murty BS, Chakraborty M (2000) Development of an efficient grain refiner for Al-7Si alloy and its modification with strontium. Mater Sci Eng A 283:94–104. doi:10.1016/S0921-5093(99)00794-7

[32] Fan Z, Wang Y, Zhang Y et al (2015) Grain refining mechanism in the Al/Al–Ti–B system. Acta Mater 84:292–304. doi:10.1016/j.actamat.2014.10.055

[33] Shaha SK, Czerwinski F, Kasprzak W et al (2016) Ageing characteristics and high-temperature tensile properties of Al–Si–Cu–Mg alloys with micro-additions of Cr, Ti, V and Zr. Mater Sci Eng A 652:353–364. doi:10.1016/j.msea.2015.11.049

[34] Jones H (2007) An evaluation of measurements of solid/liquid interfacial energies in metallic alloy systems by the groove profile method. Metall Mater Trans A 38:1563–1569. doi:10.1007/s11661-007-9171-0

[35] Gündüz M, Hunt JD (1985) The measurement of solid-liquid surface energies in the Al–Cu, Al–Si and Pb–Sn systems. Acta Metall 33:1651–1672. doi:10.1016/0001-6160(85)90161-0

[36] Jian Z, Yang X, Chang F, Jie W (2010) Solid-liquid interface energy between silicon crystal and silicon-aluminum melt. Metall Mater Trans A 41:1826–1835. doi:10.1007/s11661-010-0217-3

[37] Howe JM (1997) Interfaces in materials: atomic structure, thermodynamics and kinetics of solid-vapor, solid-liquid and solid-solid interfaces, 1st edn. Wiley, New York

[38] Tschopp MA, Coleman SP, McDowell DL (2015) Symmetric and asymmetric tilt grain boundary structure and energy in Cu and Al (and transferability to other fcc metals). Integr Mater Manuf Innov 4:11. doi:10.1186/s40192-015-0040-1